

pubs.acs.org/JACS Article

# PhotothermalPhage: A Virus-Based Photothermal Therapeutic Agent

Arezoo Shahrivarkevishahi,\* Michael A. Luzuriaga, Fabian C. Herbert, Alisia C. Tumac, Olivia R. Brohlin, Yalini H. Wijesundara, Abhinay V. Adlooru, Candace Benjamin, Hamilton Lee, Perouza Parsamian, Jashkaran Gadhvi, Nicole J. De Nisco, and Jeremiah J. Gassensmith\*



**Cite This:** https://doi.org/10.1021/jacs.1c05090



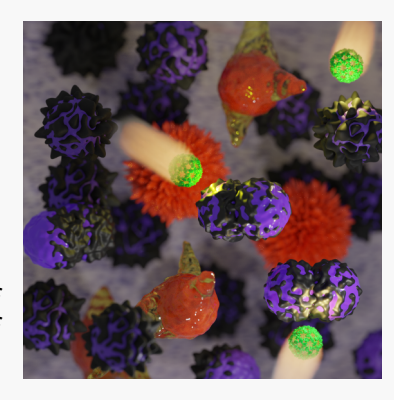
**ACCESS** 

Metrics & More



S Supporting Information

**ABSTRACT:** Virus-like particles (VLPs) are multifunctional nanocarriers that mimic the architecture of viruses. They can serve as a safe platform for specific functionalization and immunization, which provides benefits in a wide range of biomedical applications. In this work, a new generation immunophotothermal agent is developed that adjuvants photothermal ablation using a chemically modified VLP called bacteriophage  $Q\beta$ . The design is based on the conjugation of near-infrared absorbing croconium dyes to lysine residues located on the surface of  $Q\beta$ , which turns it to a powerful NIR-absorber called PhotothermalPhage. This system can generate more heat upon 808 nm NIR laser radiation than free dye and possesses a photothermal efficiency comparable to gold nanostructures, yet it is biodegradable and acts as an immunoadjuvant combined with the heat it produces. The synergistic combination of thermal ablation with the mild immunogenicity of the VLP leads to effective suppression of primary tumors, reduced lung metastasis, and increased survival time.



#### INTRODUCTION

Photothermal therapy (PTT) has emerged as a localized, noninvasive, and highly specific cancer treatment strategy that takes advantage of the heat sensitivity of cells to induce cellular death in tumors. 1-3 The cellular death and injury promote the formation of damage associated molecular patterns (DAMPs) that aid in generating a systemic immune response against tumor sites. 4-6 Typically, to achieve an efficient thermal ablation in the tumor microenvironment (TME), heating over 50 °C is required.<sup>7</sup> The induced inflammation kills cancer cells by impairing protein and DNA function in addition to turning "cold" immune-dysfunctional TMEs into "hot" immunological environments by stimulating the production and release of DAMPs that prime the formation of activated dendritic cells and promote the production of cancer killing CD8<sup>+</sup> T-cells.<sup>8,9</sup> An important factor to induce an effective immunological response in PTT treatment is using efficient photoabsorbers, particularly those that absorb light in the near-infrared (NIR) region (700– 1100 nm), where biological molecules like hemoglobin and melanin are the most transparent. 10 Organic-based photoabsorbing molecules and inorganic nanomaterials are the most commonly employed preclinical photothermal agents (PTAs) that absorb light in the NIR region and facilitate efficient heat production. 11,12 The NIR region allows for deeper light penetration through skin, and several photothermally active NIR organic molecules, such as heptamethine 13,14 and phthalocyanine, 15,16 represent an ongoing area of research. Problematically, many of these dyes, including the clinically approved indocyanine green (ICG), degrade rapidly from a selfinflicted generation of reactive oxygen species (ROS), which necessitates repeated dosing for effective PTT treatment. 17,18 One approach to overcome these issues is with the use of inorganic PTA-like nanostructures, 19 carbon nanomaterials, 20 and iron oxide nanoparticles,<sup>21</sup> which have shown strong absorption cross sections and high photothermal stability; however, metal-nanoparticles, particularly those made from gold, are generally not biodegradable and remain inside the body for long periods.<sup>22</sup> Finding a balance between high photothermal stability and pharmacokinetics is a key challenge in selecting suitable photothermal materials to simultaneously improve the therapeutic effect of PTT and fulfill its clinical efficiency. Recently, croconium dyes have shown promise as they possess high NIR extinction coefficients, low fluorescence quantum yields, and high photostability, making them promising candidates for photothermal therapy. 23,24 Indeed, recent work has shown that they have photothermal efficiencies comparable to or even surpassing those of gold nanostructures and ICG.<sup>25</sup> However, their in vivo performance is restricted by poor aqueous solubility, self-aggregation, short circulation half time, quick diffusion from tumor tissue, and rapid clearance from

Received: May 17, 2021



the body.<sup>26,27</sup> We wondered if, by combining the superior photophysical properties of the croconium system with a biodegradable nanoparticle platform, we could circumvent this problem and produce a next-generation PTT agent that induces effective thermal ablation while also adjuvanting PTT's immune-activating properties.

Virus-like particles (VLPs) are noninfectious self-assembled protein-based nanoparticles derived from the self-assembled coat proteins of viral capsids and are promising candidates for next-generation bioorganic-based photothermal agents. VLPs are biocompatible, biodegradable, thermally stable, and monodisperse and show polyvalent chemical modifiability, all of which provide unique opportunities to design bespoke compositions with programmed function. <sup>28–35</sup> Their highly organized and symmetric nature and nanometer size (20-200 nm) allow them to be taken up by toll-like receptors (TLRs) on antigen-presenting cells (APCs) as pathogen-associated molecular patterns (PAMPs) and drained to local lymph nodes to interact with immune cells. These properties have made VLPs attractive in a broad range of systems such as drug delivery, photodynamic therapy, vaccination, gene therapy, and imaging. 36-48 VLPs expressed in bacteria (i.e., *E. coli*), including bacteriophage  $Q\beta$ , incorporate nucleic acids (RNA) during the assembly process in host cells (E. coli) that can alter the adaptive immune response through the engagement of the packed RNA with different pattern recognition receptors (PRRs). Nevertheless, most VLPs are inefficient in inducing a robust cytotoxic T lymphocyte and T helper cell response by themselves. Thus, we wondered if the mild immunogenicity of  $Q\beta$  would synergistically work with NIR light-activated hyperthermia to promote a more robust anticancer immune response that combines all the positive features of gold nanostructures (efficient thermal conversion) with free Croc dyes (biodegradability).

In this work, we take advantage of the self-adjuvanting and site-specific functionalizability of bacteriophage  $Q\beta$  to engineer a photothermal and the mildly immunogenic phage (or VLP) we call PhotothermalPhage (PTPhage). The formulation is an effective photoimmunotherapy system in a triple-negative breast cancer tumor model in BALB/c mice with lung metastasis. Specifically, we show that VLP  $Q\beta$  (Figure 1A), a 30 nm icosahedral nanoparticle that can be expressed in high yields, possesses exceptional thermostability, has multiple functional handles for bioconjugation, 49-53 and serves as a powerful photothermal agent following functionalization with hundreds of croconium dyes. Not only can PTPhage sustain significant bulk photothermal heating in vitro and in vivo without denaturing, but also the nanoparticle formulation shows a significant enhancement in photothermal performance over free dye and considerable improvements in solubility. Moreover, PTPhage is taken into cells better than free croconium dye and achieves significantly greater heating in vivo than equimolar concentrations of free dye. Finally, in proof-of-principle immunological studies, we find that this contribution not only causes higher in vitro and in vivo thermal cytotoxicity but also improves T-cell and dendritic cell activation over the wellknown mildly immunomodulatory features of VLP Q\$\beta\$. 54-

#### RESULTS AND DISCUSSION

# PhotothermalPhage Synthesis and Characterization.

As shown in Figure 1A, our approach for the covalent modification of bacteriophage  $Q\beta$  begins with synthesizing a symmetric croconium dye.  $Q\beta$  VLP is composed of 180 identical

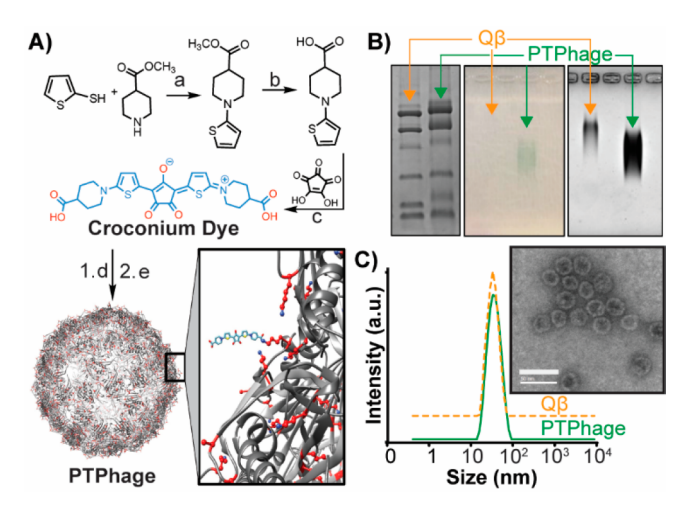
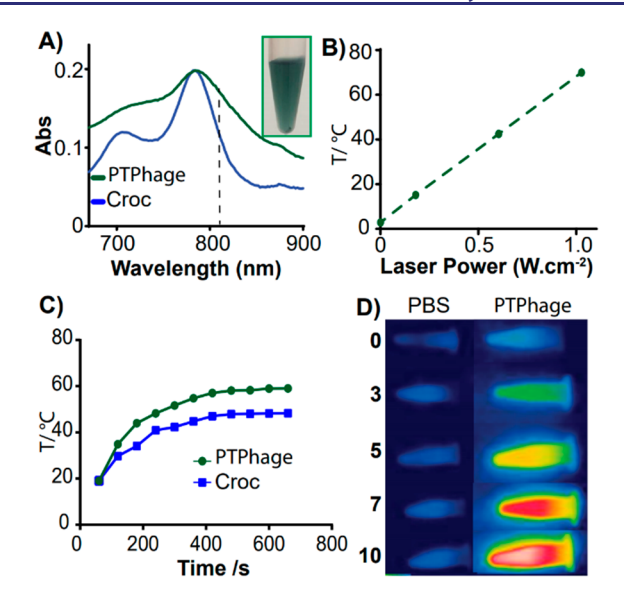


Figure 1. (A) Overall synthetic bioconjugation strategy involves synthesizing the croconium dye by (a) refluxing commercially available starting materials methyl isonipecotate and thiophene-2-thiol. (b) The resulting ester was deprotected under alkaline conditions, and (c) the final dye, Croc (thiophene-croconaine dye), was produced in the condensation reaction with croconic acid. The free acids were (d) activated as n-hydroxysuccinimide (NHS) esters and (e) added under dilute conditions to a solution of  $Q\beta$  to prevent cross-linking. The functionalized  $Q\beta$  was incubated briefly in water to hydrolyze the remaining NHS esters back to the free acid. (B) Electrophoresis mobility analysis of  $Q\beta$  before and after conjugation on SDS-PAGE (left) and agarose (center and right) gels show successful bioconjugation of dye to  $Q\beta$ . Nonreducing SDS-PAGE shows an increase in molecular weight of  $Q\beta$  after bioconjugation. The unstained agarose (center) shows a green band in bright light in the same spot in which a Coomassie-stained band (right) appears. The conjugate travels further toward the (+) electrode, which is anticipated from the replacement of lysines with carboxyl functions. (C) DLS and TEM (inset scale bar = 50 nm) of  $Q\beta$  and PTPhage demonstrate that the conjugation of croconium dye does not affect the size or polydispersity of the VLP.

capsid proteins, each with four reactive primary amine groups (three lysines and N-terminus) exposed to the outer surface, presenting a total of 720 potential sites for Croc dye labeling. Bioconjugation was employed using N-hydroxysuccinimidyl (NHS) ester activated Croc (Croc-NHS) as a site-specific and amine-reactive reagent. The resulting symmetric dye can potentially cross-link two VLPs, which produces aggregates that precipitate out of solution. To avoid this, the ratio and concentration of dye to  $Q\beta$ , incubation time, and purification procedures needed optimization. We found that 1:4 mole ratio of Q $\beta$  to dye and 12 h incubation time produced the best colloidal stability, particle size, and dye loading for our final product, PTPhage. Denaturing polyacrylamide gel electrophoresis (Figure 2B left) shows an upward shift of the subunit bands of PTPhage, indicating an increase in the molecular weight compared to  $Q\beta$ . Native agarose electrophoresis of the conjugate, which is visually seen as the blue band in the bright field image in Figure 1B center, shows greater migration toward the positive electrode compared to unfunctionalized  $Q\beta$  (Figure 1B, right), in line with the expected greater negative charge from the free carboxylates. Product morphology was confirmed by transmission electron microscopy (TEM) and dynamic light scattering (DLS) analysis (Figure 1C) at 25 °C, which shows a nearly unchanged hydrodynamic radius from unfunctionalized  $Q\beta$  (32.95  $\pm$  0.12 nm) following attachment of the Croc dye  $(33.10 \pm 0.15 \text{ nm})$ . The total number of dyes per capsid was



**Figure 2.** UV—vis spectrographic analyses of equal molar concentrations of chromophores for Croc and PTPhage show (A) a broadening of the NIR absorption of PTPhage (green line) compared to croconium dye (blue line). A photograph of PTPhage is shown in the inset. (B) A linear relationship exists between PTPhage (30  $\mu$ g·mL<sup>-1</sup>) solution temperature increases and laser power after 3 min of irradiation (laser power was set 0.0015, 0.18, 0.604, 1.02 W·cm<sup>-2</sup>). (C) Photothermal heating profiles of PTPhage and Croc at the same concentration (30  $\mu$ g mL<sup>-1</sup>) after 11 min of laser irradiation (808 nm, 0.18 W·cm<sup>-2</sup>) show a significant difference in temperature increase (40.1 °C for PTPhage and 29.1 °C for Croc). (D) Temperature variations of PTPhage and PBS under laser irradiation are mapped and quantified by a thermal camera. No noticeable temperature increase was observed in PBS under the 808 nm laser irradiation (0.18 W·cm<sup>-2</sup>) at different time points.

determined to be approximately 1.2 by UV—vis analyses, giving an average of 212 dyes per VLP.

Dyes used in PTT are most efficient when they are intensely colored and cannot dissipate energy through radiative relaxation pathways, e.g., fluorescence, electron transfer, or intersystem crossing. Croc is well suited for this as it has strong NIR absorption ( $\lambda_{\rm max}=783$  nm,  $\varepsilon_{\rm max}=2.0\times10^5$  mol $^{-1}$  cm $^{-1}$  in water), sengligible fluorescence, and low oxygen photosensitization, which also improves its photostability, a known issue with ICG and the extensively investigated heptamethine dyes. We were pleased to find that PTPhage exhibits a strong NIR absorption maximum ( $\lambda_{\rm max}=783$  nm) identical to that of free croconium dye, yet the absorption spectrum is significantly broadened (Figure 2A). This broadening is pronounced in the NIR region, which promotes more efficient conversion of clinically used lasers (emissions centered at 808 nm).

This effect was made apparent when we compared the bulk solution photothermal response of PTPhage and free dye. Both solutions containing an identical concentration of chromophore ( $30~\mu g \cdot m L^{-1}$ ) were fitted with a thermocouple and placed in front of a thermal camera. Temperature change in each solution was monitored over 11 min of laser irradiation at 808 nm and 0.18 W·cm<sup>-2</sup>. As seen in Figure 2C, the solutions showed a marked difference in heating rates and maximum temperature with PTPhage showing a  $\Delta T$  of 40.1 °C and a  $T_{\rm max}$  of 59.1 °C compared to free dye ( $\Delta T = 29.9$  °C;  $T_{\rm max} = 48.5$  °C). Additional laser irradiation experiments have been done to investigate photothermal properties of PTPhage at different laser powers (0.0015, 0.18, 0.604, and 1.02 W·cm<sup>-2</sup>), times of

radiation (1–10 min), and various concentrations (0.1–1 mg·mL<sup>-1</sup>) of PTPhage. For instance, we found an increase in the bulk temperature of the solution that is linear with laser power (Figure 2B and Figure S10). Collectively, the PTPhage appears to have superior photothermal properties compared to free dye, which allows for lower laser power density and dye concentration, potentially reducing side effects on normal tissue. To show that the 808 nm laser does not change the temperature of the water itself, we irradiated a solution of buffer and PTPhage (Figures 2D and S10) and observed no temperature change in the PBS solution, whereas we could heat a solution of PTPhage from room temperature to 61 °C with an 808 nm laser at 0.18 W·cm<sup>-2</sup>.

The photothermal stability of the PTPhage complex was proven by comparing size distribution, absorption, and size exclusion chromatography before and after 10 min of continuous laser irradiation (0.18  $\rm W \cdot cm^{-2}$ ) as shown in Figure 3A–D. The results showed no photobleaching, aggregation, or

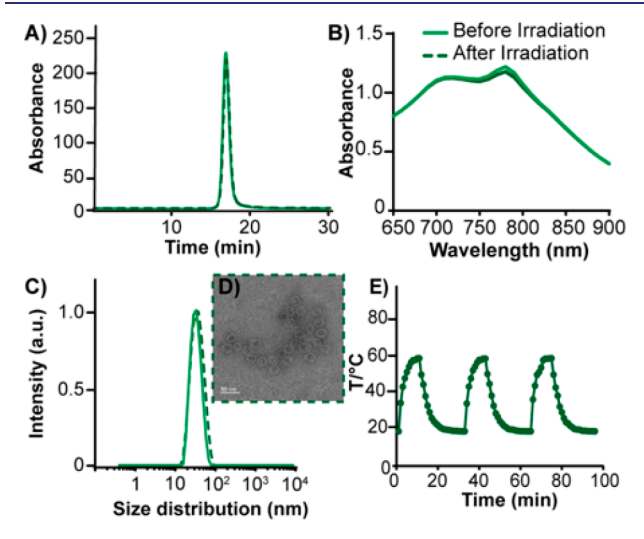
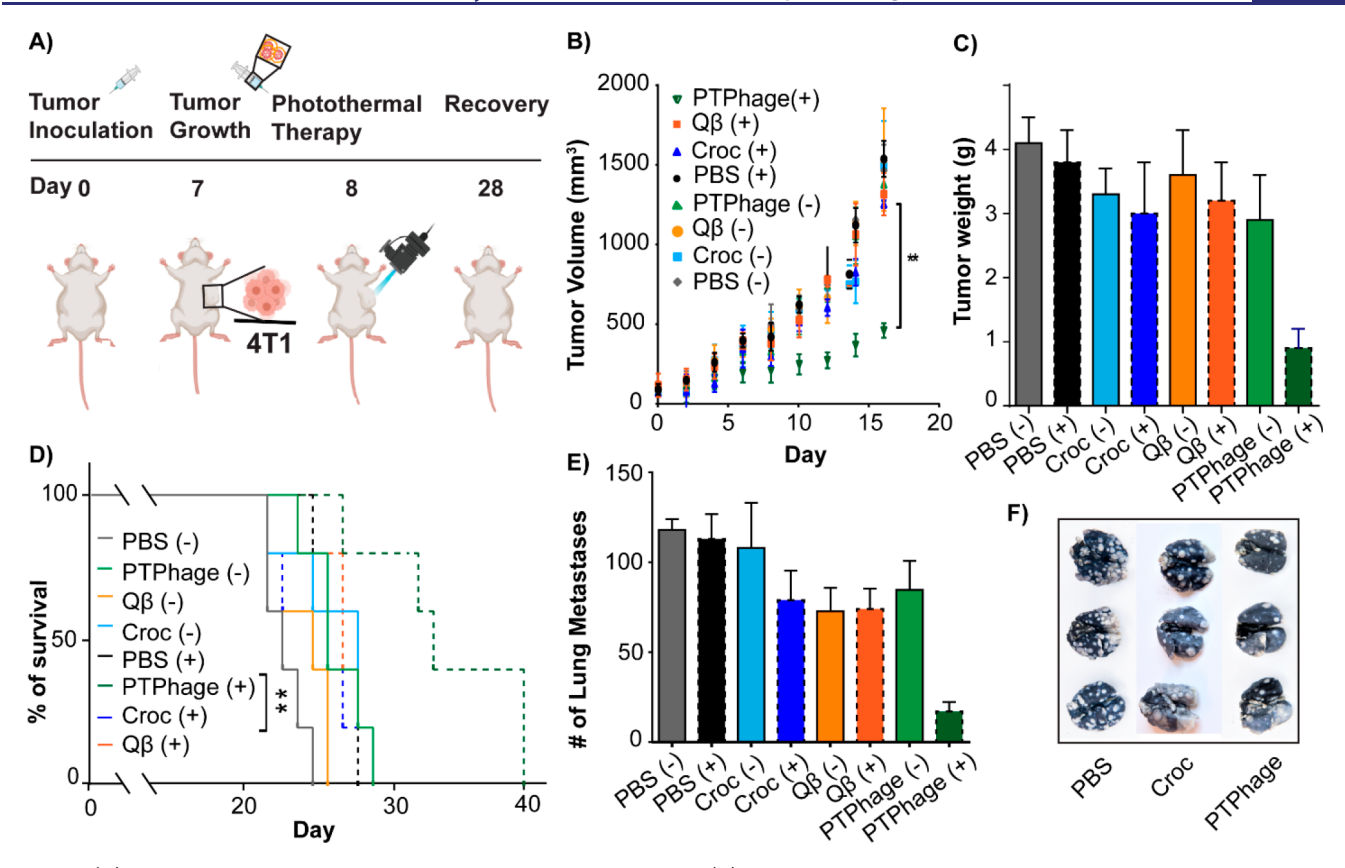


Figure 3. (A) Photothermal stability of PTPhage after 10 min of laser irradiation (0.18  $W\cdot cm^{-2}$ ) is shown by intact HPLC profile of PTPhage before and after radiation. (B) No significant change in absorption spectra of PTPhage after laser-induced heating for 10 min. (C) DLS and (D) TEM data (scale bar is 50 nm) prove thermal stability of PTPhage with no morphology change after 10 min of laser irradiation. (E) Thermal cycling of PTPhage shows no change in heating profile after three cycles.

structural change, indicating high photostability of the system. To demonstrate the remarkable stability of the PTPhage, we performed a thermal cycling experiment. A PTPhage solution (30  $\mu$ g·mL<sup>-1</sup> of Croc concentration) was irradiated repeatedly (808 nm, 0.18 W·cm<sup>-2</sup>), and the temperature was monitored over the heating and cooling cycles, as shown in Figure 3E. The PTPhage showed impressive photothermal durability; we tested its photothermal behavior by radiating a single sample for 10 min intervals over 10 days and monitored the heating and cooling curve (Figure S11) and found no obvious change in the maximum temperature or cooling curve. In line with strong absorbance in the NIR region and high photostability, we further determined the photothermal efficiency of the PTPhage and compared it with existing photothermal materials: free Croc dye and gold nanorod (AuNR). 59 We found that the PTPhage has higher photothermal conversion efficiency (77%) compared to Croc alone (70%) and AuNR (68%), which is in line with the literature (Figure S12). From these results, we believe that the



**Figure 4.** (A) Experiment design of synergistic immunophotothermal therapy. (B) Tumor growth curves of 4T1 tumor-bearing mice treated with PBS,  $Q\beta$ , Croc, and PTPhage with and without laser radiation showing the most effective therapeutic approach is attributed to PTPhage which exhibited the greatest restriction to tumor growth. (C) Tumor weight as a representative of tumor suppression verified high antitumor performance of PTPhage compared to Croc,  $Q\beta$ , and PBS groups. (D) Survival study of 4T1 tumor-bearing BALB/c mice (n = 5). (E) Number of lung nodules after India ink staining. (F) Representative images of India-ink-infused lungs of irradiated Croc, PTPhage, and PBS mice with white spots clearly demonstrate number of metastatic nodules per each group. \*\*p < 0.05.

high photostability, durability, and remarkable photothermal conversion efficiency of PTPhage make it a good candidate for PTT.  $^{60}\,$ 

PhotothermalPhage in Vitro Cytotoxicity. Cellular uptake of both PTPhage and free Croc was assessed on 4T1 (murine breast cancer) cells. Because Croc lacks fluorescence, we determined uptake by measuring the amount of remaining dye in the supernatant after a 4 h incubation period. In a typical experiment, PTPhage and Croc were added to cell media in equal chromophore concentrations, and after 4 h, the cells were removed, the media filtered, and the total absorption at the  $\lambda_{\rm max}$ was compared before and after. All concentrations were within the linear range of Beer's law, allowing direct calculation of before and after concentrations. As shown in Figure S13, cellular uptake of PTPhage is about twice that of croconium dye. Croc, being negatively charged, is very unlikely to partition into the cell, and so these results were not surprising. Next, for the *in vitro* phototoxicity in 4T1 cells, the photoablation efficiency of PTPhage and Croc was determined by incubating identical concentrations (3.1  $\mu$ g·mL<sup>-1</sup>) in cell culture. After 4 h incubation at 37 °C, cells were washed with PBS and fresh phenol red-free media to remove any remaining dye. Before laser irradiation, the microwell plate was equilibrated to 37 °C, as it has been shown in previous studies that initial temperature (RT vs 37 °C) has a significant effect on the in vitro PTT efficiency. All four experimental groups were exposed to an 808 nm laser for 10 min (0.18 W·cm<sup>-2</sup>). The next day, cell viability in each well was determined by MTT assay. As shown in Figure S14, all

formulations before laser radiation showed low toxicity, whereas the cell viability of PTPhage dropped dramatically to 17% while free Croc dropped to only 65% after laser radiation. We attribute this greater cell killing to the improved cellular uptake and therefore greater intracellular heating. These results were qualitatively confirmed through visual analyses of cell viability via a live/dead cell assay (Figure S14). With these results in hand, we conducted *in vivo* antitumor studies to see if we would observe a similarly improved response with PTPhage. To further check the biocompatibility of the formulation, we tested cell viability in two different cancer cell lines, 4T1 breast cancer and T42 epithelial bladder cancer cells, after treatment with PTPhage, Croc, and  $Q\beta$  using LDH cytotoxicity assay. As shown in Figure S15 and Figure S16 there was no sign of toxicity in the PTPhage group.

Photothermal Antitumor Response in Vivo. We assessed the antitumor effect of our system in the same murine mouse cancer model discussed above. 4T1 cells  $(1 \times 10^6)$  were implanted into the abdominal mammary gland of 4- to 6-week-old female BALB/c mice. One day before injection, the fur was removed from the spot of injection (tumor site) for better monitoring of tumor growth and tumor volume measurement using calipers. Tumor development was allowed to proceed until the average tumor size reached 5–6 mm, after which mice were randomly divided into four groups with radiation and four groups without radiation for various treatments: PBS (negative control),  $Q\beta$ , and identical concentrations (by chromophore) of Croc and PTPhage. Following randomization, mice from each

group (n = 5) were injected intratumorally  $^{61}$  (50  $\mu$ L) in a single location in the tumor site using an insulin syringe. We allowed 2 h for the injections to diffuse through the tumor microenvironment, and then laser treatment was performed (808 nm, 0.18 Wcm<sup>-2</sup>,10 min) as schematically shown in Figure 4A and the tumor temperature was monitored using a thermal camera (Figures S18 and S19). Intratumoral injections with photoactive therapeutics make sense since the tumor must be accessible for irradiation. The effect of treatment was evaluated by monitoring the body weight of the mice and measuring tumor volume over 16 d. Tumor volumes were measured using calipers every other day after treatment and calculated according to the equation Vol = (tumor length)  $\times$  (tumor width)  $\cdot$  2/2. The tumors treated with PTPhage plus laser irradiation developed a sizable black scab on the tumor site and showed slower tumor growth compared to all other experimental groups. The bodyweight of each group was monitored over 16 d, and we found no significant change, which suggests PTPhage,  $Q\beta$ , and Croc did not induce toxicity (Figure S20). Furthermore, to observe pathological toxicity, H&E staining of the major organs of the mice including heart, liver, lung, and kidney was performed after treatment of the mice with PTPhage, Croc, Q $\beta$ , and PBS. As shown in Figure S17 neither adverse effects nor significant histological abnormality in the treatment group was found, suggesting high biocompatibility of our formulation. The irradiated Croc dye and  $Q\beta$  by itself slightly delayed the growth of the primary tumor though nowhere near as much as the PTPhage formulation, which caused obvious tumor ablation after NIR laser exposure. The degree of tumor ablation and recission induced by different groups was further confirmed through tumor volume and tumor weight Figure 4B,C. As shown in Figure 4D, PTPhage again produced significant suppression on tumor growth compared to  $Q\beta$  and Croc alone. H&E and TUNEL staining of the tumor showed lower nuclei count and cell density as well as the highest apoptosis of tumor cells in PTPhage compared to other groups (Figure S22). Survival of the different groups of treated tumorbearing mice was studied over 38 d following the initial tumor inoculation. As shown in the Kaplan-Meier survival curve, illustrated in Figure 4E, only PTPhage prolonged survival time compared to other groups. Metastatic burden was evaluated at day 16 post-treatment by removing the lungs and staining them with India ink, which preferentially blackens healthy tissue making the metastasis stand out. Control groups (PBS) and unirradiated free Croc show statistically identical tumor burdens, as illustrated in Figure 4E, Figure 4F, and Figure S21. The unaltered  $Q\beta$  and irradiated free Croc groups all produced a modest and statistically significant decrease in metastatic burden. Summarily, the antitumor activity of PTPhage appears to be improved over free Croc.

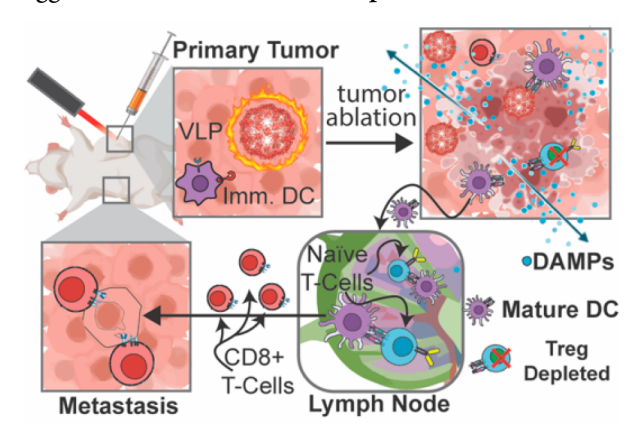
Immunological Studies. While the scope of this work is primarily the synthesis and antitumor response of PTPhage, we wondered if the VLP was enhancing the immunological response initiated by the PTT. Detailed antitumor immunological studies will be addressed in subsequent work. Our initial focus in this part of the study was the assessment of dendritic and T-cell activation and an assessment of any downregulation of protective T-cell (Treg) response. In antitumor immunity, dendritic cells (DCs) are an important and effective class of APCs that play a pivotal role in initiating and regulating innate and adaptive immunities. Generally, immature DCs ingest foreign materials through different surface receptors, including pattern recognition receptors that trigger their maturation. APRs detect PAMPs (derived from microorganisms) and

DAMPs (produced by the body's dying cells). Mature DCs can process antigens into peptides for presenting on major histocompatibility complex class I/II (MHC-I/II) molecules that coincide with increased expression of B7-1/CD80 and B7-2/CD86 co-stimulatory molecules. Following maturation and antigen exposure, DCs migrate into the draining lymph node (where contact is mediated between DCs and T-cells) and promote the differentiation and proliferation of naive T-cells into cytotoxic T lymphocytes (CTLs), which are key effector cells for anticancer immunity. 9,65-67 Only mature DCs can elicit antitumor effector T-cell responses, which can be determined by assessing DC maturation in vitro following exposure to an antigen. It is well-known that VLPs mimic viruses in their size, structure, and antigenic epitopes. Their 20–200 nm size is in the optimal diameter range that can directly drain to the lymph node. In addition, because of their regular polyhedron structure and highly repetitive surface feature, VLPs are sensed as PAMPs by PRRs on the surface of DCs. Furthermore, the encapsulated nucleic acids also can be recognized by PRRs and promote DC maturation for priming CD4+ T helper lymphocytes and CD8+ cytotoxic T lymphocytes. 56 These cytotoxic T-cells can then fight systemic cancer at metastatic

We first investigated whether  $Q\beta$  stimulates the maturation of DCs by using cultured bone marrow derived DCs (BMDCs) separated from BALB/c mice and incubating them with different concentrations of  $Q\beta$  for 24 h. The expression of DCs maturation markers (proteins called CD80 and CD86) were determined by staining them with anti-CD80 and anti-CD86 fluorescent antibodies and quantifying them using flow cytometry (FCM). We found that  $Q\beta$  upregulates the expression of CD86 and CD80 and enhances the percentage of matured DCs (CD11c+CD80+CD86+) in BMDCs at all concentrations tested compared to PBS (Figure S23). Next, we focused on evaluating the adaptive immunity triggered by  $Q\beta$  at cellular levels after incubation with splenocytes harvested from a naive mouse. Again,  $Q\beta$  was mildly able to promote the effector CD4<sup>+</sup> T helper lymphocytes (CD4<sup>+</sup>CD3<sup>+</sup>CD44<sup>+</sup>CD62L<sup>-</sup>) and CD8<sup>+</sup> cytotoxic T lymphocytes (CD8<sup>+</sup>CD3<sup>+</sup>CD44<sup>+</sup>CD62L<sup>-</sup>), which show possible immunoadjuvant potential of  $Q\beta$  in the PTPhage system to stimulate antitumor immune responses (Figure S23).

PTT induces apoptosis and necrosis, efficiently destroys tumor cells, subsequently releasing debris containing tumorassociated antigens and chemokines. 70,71 These antigens are subsequently taken up by DCs and trafficked to the lymph node, triggering antitumor immune responses. Furthermore, DAMPs released from necrotic cancer cells, such as heat shock proteins, calreticulin, and ATP, can also promote DC maturation and assist in activating effector CD8<sup>+</sup> T-cells that enter circulation to fight against primary and metastatic sites systemically (Scheme 1).6,72 Our data show that Q $\beta$  can simultaneously act as an immunological agent to promote DC activation and enhance infiltration of CTLs. As shown in Figure 2C, PTPhage and Croc both show favorable photothermal effects in a wide temperature range (40-60 °C); thus, we set up our in vivo experiment to evaluate immunostimulatory activities of the combinational formulation compared to PTT alone. BALB/c mice were inoculated with 4T1 cells and grown until they had a primary tumor size of 100 mm<sup>3</sup>. The mice were separated into four groups (n = 5) and injected with PBS, Q $\beta$ , Croc, or PTPhage (same dye concentration as free Croc). Two hours postinjection, they were irradiated with 808 nm laser for 10 min

Scheme 1. Illustration of PTPhage-Initiated Photothermally Triggered Antitumor Immune Response<sup>a</sup>



"An initial photothermal excitation of the VLP causes an increase in temperature, which results in local tissue ablation. This causes local apoptosis/necrosis and the release of immune-stimulating DAMPs. The presence of intact VLP in the ablated tumor environment simulates a potential infection, which causes downregulation of the immunosuppressive response by suppressing Treg cell formation. These responses can be measured in the draining lymph node. In this lymph node, cancer antigens collected by activated dendritic cells can present to naïve T-cells, which mature to cytogenic CD8+ cells. These cells can then attack metastatic lesions.

(0.18 W·cm<sup>-2</sup>). We conducted our experiment initially by assessing identical concentrations (the same number of NIR dyes) of PTPhage and free Croc as measured by UV-vis. The temperature at the tumor surface ends up being higher for PTPhage (54  $\pm$  2 °C) compared to free Croc (40  $\pm$  1 °C) (Figures S18 and S19), which can be ascribed to a more rapid clearance of free Croc from the tumor and greater photothermal efficiency of PTPhage at 808 nm. Three days post-treatment, the mice were sacrificed, and the spleen and draining lymph node were collected to analyze the T lymphocytes and mature DCs by flow cytometry after co-staining with various markers. It is worth noting that post-PTT the populations of immune cells within the tumors were all very low, likely from the photoablation, and getting useful data from the tumors was difficult. Since our interest is in studying how PTPhage adjuvants the effects of ablative PTT, this was anticipated. We were able to get statistically meaningful data from the draining lymph and spleen; however, these populations are generally useful in measuring local and systemic immune response in cancers. 73,74 The percentage of matured DCs (CD11c+CD80+CD86+) in the draining lymph node from PTPhage was 24% greater than the Croc group, as shown by higher expression of costimulatory molecules CD80 and CD86 (Figure 5A), validating PTPhage's in vitro behavior and showing it can enhance the activation of APCs better than each formulation alone. We also determined how PTPhage affects CD8<sup>+</sup> T-lymphocyte cells in the draining lymph node and found a significant number of activated (CD44+CD62L-) CD8+ T-cells in the PTPhage group compared to other treated groups (Figure 5B). The number of activated CD4+ and CD8+ was also determined in spleen (Figure 5C,D), and a significant increase was found in the group treated with PTPhage. To exclude the effect of the more efficient photothermal and tumor residency of PTPhage, we analyzed DCs' maturation in the draining lymph node when tumor tissue temperature for both PTPhage and Croc group reached the same temperature after laser irradiation (this required different

amounts of dye in each formulation). Multiple studies show that heating tumor cells at low temperature (39.5–44 °C) enhances blood flow in the tumor and improves the permeability of tumor vasculature and may promote better migration of DCs between tumor and lymphoid organs even if it is not as efficient as a higher temperature range (>45 °C) in destroying the primary tumor. Therefore, we utilized 1.5  $\mu$ g·mL<sup>-1</sup> PTPhage and 4 times the amount of Croc (6.0  $\mu$ g·mL<sup>-1</sup>) to produce a final tumor temperature of approximately 44 °C and maintained this temperature for 10 min by 808 nm laser irradiation. Intriguingly, as shown in Figure 5E,F, we observed the same general trends where PTPhage outperforms free dye significantly in stimulating DC and T-cells. Consequently, we do not think that temperature alone explains the antitumor results reported above.

We next assessed T-cell responses to PTPhage. The population of activated effector CD8+ cytotoxic T-cell (CTL, CD8<sup>+</sup>CD44<sup>+</sup>CD62L<sup>-</sup>) and activated CD4<sup>+</sup> T-helper cells (T<sub>H</sub>, CD4<sup>+</sup>CD44<sup>+</sup>CD62<sup>-</sup>) were quantified in spleens by FCM after various treatments. Compared to either Croc or  $Q\beta$  alone, the combination treatment resulted in 2.10-fold increase in helper CD4<sup>+</sup> T-cell and 2.12-fold increase in CTL CD8<sup>+</sup> T-cells compared to Croc (p < 0.05) (Figure 5E-H). These results collectively demonstrate that PTPhage can act as a powerful photothermal agent along with potentiating PTT's immunological response. The single-cell suspensions of spleens from four different groups of mice were stained with anti-CD3 instead of anti-CD11c, -CD4, -CD44, and -CD62L antibodies to measure how much effector T-cells were expressed after each treatment. As displayed in Figure 5G,H, significant CD4<sup>+</sup>CD44<sup>+</sup>CD62<sup>-</sup> cells appeared for mice treated with PTPhage. One limitation in most of radiotherapy systems is that, following tissue damage, the tumor microenvironment can develop immunosuppressive cells, which creates an immunological "cold" tumor that restricts the therapeutic performance. 8,75,76 Several studies have reported that the efficiency of PTT inversely correlates with Treg cells, an immunosuppressive subset of CD4<sup>+</sup> T cells characterized by the expression of factor forkhead box protein P3 (FoxP3).

Necrotic cell death induced by PTT causes an inflammatory response that promotes the expression of Treg immunosuppressive molecules to prevent the initiation of a strong systemic immune response. We expected that  $Q\beta$  may amplify the immune response, and its presence as a foreign viral protein might "trick" the immune system into turning off this immunosuppressive response. Therefore, we assessed the presence of CD4+FoxP3+ after different treatments by flow cytometry to investigate the ratio of the effector CD4<sup>+</sup> T-cells vs Treg in the spleen, an organ that serves as a systemic repository for the immune system. As expected, and shown in Figure 5I,J, PTT alone produces a suppressive environment while PTPhage (a combination of PTT and the immunoadjuvanting agent  $Q\beta$ ) decreased the percentage of Tregs (lower CD4+FoxP3+). This is significant because cancer therapeutic efficacy is associated with tumor suppression and higher survival time correlates with lower Tregs and higher effector T-cells.

## CONCLUSION

In this work, we took advantage of VLP  $Q\beta$ 's biocompatibility, functionalizability, and modest immunogenicity to produce a new synthetic biomaterial hybrid PTT "PTPhage". This formulation significantly improved the photophysical properties of Croc, including photothermal conversion efficiency and water solubility, as shown by an enhancement of cellular death upon

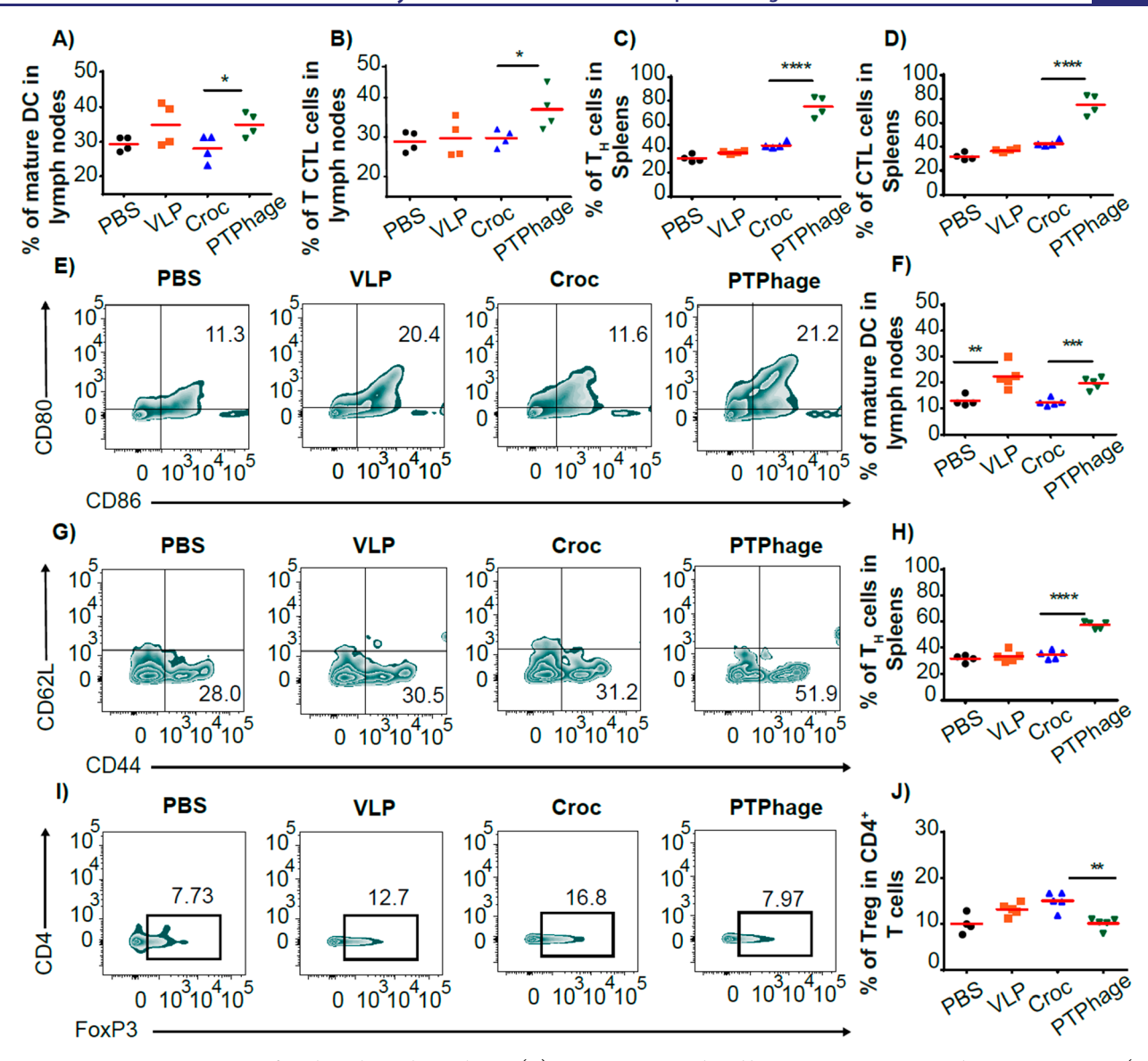


Figure 5. In vivo immune responses after photothermal stimulation. (A) DC maturation induced by various groups on mice bearing 4T1 tumors (gated on CD11c<sup>+</sup> DC cells, Figure S24) after PTT treatment ( $T_{\rm max}$  = 54.2 °C). Cells in the tumor-draining lymph node were assessed by flow cytometry after staining for CD80 and CD86 expressions. (B) Quantification of CTLs (CD8<sup>+</sup>) in isolated lymph nodes. (C, D) Percentage of activated  $T_{\rm H^-}$  cells (CD4<sup>+</sup>CD44<sup>+</sup>CD62<sup>-</sup>) and CTLs in spleens. Single-cell suspensions were processed from the spleen and analyzed by flow cytometry after anti-CD3, -CD4, -CD8, -CD44, and -CD62L staining ( $T_{\rm max}$  = 54.2 °C). (E, F) Representative flow cytometry plots showing expression of CD86 and CD80 on DC of draining lymph node for different groups (gated on CD11c<sup>+</sup>, Figure S24) after PTT treatment ( $T_{\rm max}$  = 44.0 °C). (G, H) Representative flow cytometry plots of effector CD4<sup>+</sup> in spleen cells of different treatment groups analyzed by flow cytometry (stained with anti-CD3, -CD4, -CD44, and -CD62L) ( $T_{\rm max}$  = 44.0 °C). (I, J) Representative flow cytometry plots showing percentages (gated on CD4<sup>+</sup> cells, Figure S24) of CD4<sup>+</sup>FoxP3<sup>+</sup> T cells in the spleen after various treatments.

808 nm laser exposure than free dye. In addition, this synergistic combination showed excellent NIR light-induced tumor ablation by suppressing 70% of the primary breast cancer tumor in BALB/c mice bearing a highly metastatic 4T1 tumor compared to 18% for Croc alone. PTPhage also prolonged survival time and reduced lung metastasis by 85% compared to control. Our initial immunological screening strongly suggests that the VLP may adjuvant PTT by promoting greater DC, Thelper, and cytotoxic T-cell responses while lowering immunosuppressive Treg cells. These results are intriguing, and studies that combine effective Th1 promoting adjuvants, lower intratumoral temperatures, and checkpoint inhibitors to promote these effects even more are underway.

#### EXPERIMENTAL SECTION

Expression Protocol of Endotoxin Free ClearColi  $Q\beta$ . Expression and purification of  $Q\beta$  were done as reported elsewhere and slightly modified as described below. The plasmid used was a kind gift from Dr. M. G. Finn from the Georgia Institute of Technology. Competent endotoxin free ClearColiBL21 DE3 *E. coli* single colonies were mixed with 100 mL of SOB media supplemented with kanamycin  $(50\,\mu\mathrm{g\cdot mL^{-1}})$  and incubated overnight at 37 °C. Grown cells were then amplified to 2 L of media, and OD600 was monitored for 4 h and bacteria induced using 1 mM of isopropyl  $\beta$ -D-1-thiogalactopyranoside (IPTG) when the optical density reached ranged a value of 0.9. Induced bacteria were incubated for 12 h at 37 °C. Cells were then harvested by centrifugation (19 510g) at 4 °C for 30 min, then lysed using a cell homogenizer. Lysate was centrifuged for 1 h at 4 °C (19 510g), supernatant collected, and protein salted-out by mixing with 2 M

ammonium sulfate at 4 °C for 12 h. Protein was then collected under centrifugation (19 510g) for 30 min at 4  $^{\circ}$ C and resuspended in 0.1 M potassium phosphate buffer, pH 7.0. Excess lipids and membrane proteins were extracted by mixing with equal volumes of *n*-butanol and chloroform. The resulting aqueous layer was purified under sucrose gradients (10–40%) for 12 h (87 808g). Purified Q $\beta$  was pelleted upon centrifugation for 4 h (179 200g) and characterized by TEM, agarose gel, and dynamic light scattering (Figure S2).

Electroporation of ClearColi Qβ. ClearColi cells were transformed with a pET28 plasmid carrying the coat protein sequence of  $Q\beta$ . Electrocompetent cells were thawed on ice for 10 min and mixed by gentle pipetting. Then, 25  $\mu$ L of thawed competent reaction cells was transferred into a 1 mL microcentrifuge tube. Further, 1  $\mu$ L of the Q $\beta$ plasmid was added to the cell suspension. The resulting mixture was chilled within an electroporation cuvette for 5 min. Electroporation was done at 25  $\mu$ F, 100  $\Omega$ , and 2.1 kV for approximately 2.6 ms. The electroporated cells were immediately mixed with 475  $\mu$ L of prewarmed (37 °C) SOB media inside the electroporation cuvette. The mixture was gently swirled twice and then transferred to a sterile culture tube (3 mL). Bacteria were shaken under 250 rpm at 37  $^{\circ}$ C for 60 min. Finally, bacteria were plated into LB media plates supplemented with kanamycin for 12 h.

Synthesis of Croconium Dye. Croconium NIR dye was synthesized according to a previously described method.<sup>2</sup> The synthetic route is shown in Figure 1A. Briefly 4.30 g (30.0 mmol) of methyl isonipecotate and 2.32 g (20.0 mmol) of thiophene-2-thiol were mixed in 20 mL of toluene and refluxed for 2 h. After cooling down to room temperature, the reaction mixture was filtered through a silica gel and washed with ethyl acetate. The resulting compound methyl 1-(thiophen-2-yl)piperidine-4-carboxylate (compound a) was obtained as a pale-yellow solid with 64% yield.  $^1\! H$  NMR (600 MHz, acetone)  $\delta$ 6.75 (dd, J = 5.5, 3.7 Hz, 1H), 6.65 (dd, J = 5.5, 1.3 Hz, 1H), 6.16 (dd, J = 3.7, 1.3 Hz, 1H), 3.54 - 3.47 (m, 3H), 2.89 - 2.79 (m, 2H), 2.50 (tt, J = 3.7, 1.3 Hz)11.2, 3.9 Hz, 1H), 2.07 (t, J = 2.2 Hz, 2H), 2.03–1.96 (m, 2H), 1.81 (dtd, J = 13.3, 11.3, 4.0 Hz, 2H) (Figure S3). <sup>13</sup>C NMR (151 MHz, acetone) δ 175.24, 160.34, 126.89, 112.71, 106.22, 52.06, 51.82, 40.91, 28.45 (Figure S4). Next, 0.45 g (2.0 mmol) of compound a was dissolved in 10 mL of 0.5 M sodium hydroxide solution and was refluxed for 1 h. The pH of the reaction mixture was acidified with 10% acetic acid to obtain [1-(thiophen-2-yl)piperidine-4-carboxylic acid] (compound b), a white precipitated form with 74% yield. <sup>1</sup>H NMR (600 MHz, MeOD)  $\delta$  6.75 (dd, J = 5.4, 3.7 Hz, 1H), 6.66 (dd, J = 5.5, 1.3 Hz, 1H), 6.20 (dd, J = 3.7, 1.3 Hz, 1H), 3.51 (dt, J = 12.9, 4.1 Hz, 2H), 2.83 (td, J = 11.8, 2.9 Hz, 2H), 2.44 (tt, J = 11.2, 3.8 Hz, 1H), 2.02 (dddd, *J* = 13.2, 5.8, 3.7, 1.9 Hz, 2H), 1.85 (dtd, *J* = 13.4, 11.4, 4.1 Hz, 2H) (Figure S5).  $^{13}$ C NMR (151 MHz, MeOD)  $\delta$  178.76, 160.80,126.67, 107.56, 53.12,44.59, 41.77, 30.66, 29.03 (Figure S6).

Subsequently, 0.142 g (1.00 mmol) of croconic acid was mixed with 0.422 g (2.00 mmol) of compound **b** and dissolved in the mixture of *n*butanol and toluene (30 mL, 1:1). The reaction was stirred for 1 h under reflux. After cooling down to room temperature, the mixture was filtered and washed with methanol and the product was dried under vacuum to obtain pure croconium dye as a black solid (yield 67%). <sup>1</sup>H NMR (600 MHz, DMSO)  $\delta$  12.40 (s, 2H), 8.50 (s, 2H), 7.05 (d, J = 5.0Hz, 2H), 4.00 (dt, J = 13.6, 4.3 Hz, 4H), 3.53 (t, J = 11.6 Hz, 4H), 2.67(tt, J = 10.7, 4.0 Hz, 2H), 2.08-2.02 (m, 4H), 1.79-1.65 (m, 4H)(Figure S7).  $^{13}$ C NMR (151 MHz, DMSO)  $\delta$  184.69, 181.54, 174.99, 122.54, 114.59, 50.66, 42.52, 30.69, 27.47, 24.65 (Figure S8). ESI) *m/z*:  $[M + Na]^+$  calculated for  $C_{25}H_{24}N_2O_7S_2$ , 551.57; found, 551.10.

EDC/NHS Coupling Reaction on Croconium Dye. Croconium dye (150.0 mg, 0.2800 mmol), N-hydroxysuccinimide (0.097 g, 0.85 mmol), and EDC (0.13 g, 0.85 mmol) in DMF 6 mL were stirred at room temperature 24 h. The DMF was removed under reduced pressure followed by dissolving the remaining residue in 20 mL of EtOAc. The organic layer was washed with water  $(3 \times 20 \text{ mL})$ , dried with MgSO<sub>4</sub>, and concentrated under reduced pressure (yield 54%). <sup>1</sup>H NMR (600 MHz, DMSO)  $\delta$  8.53 (s, 2H), 7.08 (s, 2H), 4.06 (d, J = 13.6 Hz, 4H), 3.63 (t, J = 12.3 Hz, 4H), 2.79-2.72 (m, 8H), 2.59 (d, J = 16.6Hz, 2H), 2.20 (d, J = 13.1 Hz, 4H), 1.90 (d, J = 11.8 Hz, 4H) (Figure S9).  $^{13}$ C NMR (151 MHz, DMSO)  $\delta$  175.46, 173.23, 170.64, 170.13,

162.78, 73.73,51.16, 50.53, 36.99, 36.25, 34.03, 31.61, 31.24, 29.47, 27.96, 25.70, 22.47, 21.37.

**Bioconjugation.** A solution of  $O\beta$  VLPs (1 mg·mL<sup>-1</sup> in 0.1 M phosphate buffer, pH 7) was treated with a premixed DMSO solution (10%) of Croc-NHS (final concentration 0.05 mM) in the mole ratio of 1:4 Q $\beta$  to dye. The solution was incubated for 12 h at room temperature, and the nonconjugated dye from the sample was removed by 10 kDa cut-off centrifugal column and then running the collected fraction through a Sephadex 25G column. Protein concentration was determined by Bradford assay. Bioconjugation efficiency was determined based on absorption spectroscopy using the Lambert-Beer law: absorbance (A) = extinction coefficient ( $\varepsilon$ ) × molar concentration (c)  $\times$  path length (l). A UV-vis spectrum of the conjugate solution was obtained (one should remember to dilute the solution to an absorbance of <1.0 for an accurate measurement).  $A_{\text{max}}$ was measured at the maximum wavelength ( $\lambda_{max} = 783$  nm) of croconium dye with extinction coefficient of  $2.0 \times 10^{5}$  mol<sup>-1</sup> cm<sup>-1 57</sup> to obtain a concentration of bound dye by  $c = A_{\text{max}}/(\varepsilon l)$ . Q $\beta$  concentration was obtained by Bradford assay, the mole ratio of dye to  $Q\beta$  in PTPhage was calculated, and a total of 212 dyes were attached at approximately 720 potential conjugation sites.

Animal Model and Cell Preparation for Tumor Injection. The female BALB/c mice (6 weeks, 18-23 g) were purchased from Charles River Laboratories. Study protocol (no. 18-17) was approved by the Institutional Animal Care and Use Committee of The University of Texas at Dallas. 4T1 tumor models were established by subcutaneous injection of 1× 10<sup>6</sup> 4T1 cells on mammary fat pad of BALB/c mice as prepared: 4T1 breast cancer cells cultured in RPMI 1640 medium supplemented with 10% fetal bovine serum and 1% penicillinstreptomycin were trypsinized and washed 3× with 1× PBS. 50 µL of  $\sim 1.0 \times 10^6$  cells suspended in 1:1 mixture of PBS and Matrigel (high concentration phenol red free purchased from Corning).

Single Cell Suspension. On day 3 post-treatment, the spleens and lymph nodes were collected from each mouse and brought into a single cell suspension. Briefly, the spleens and lymph nodes were shredded with tweezers and passed through a cell strainer using RPMI 1640 medium supplemented with 10% FBEssence, 1% penicillin-streptomycin, and 50  $\mu$ M  $\beta$ -mercaptoethanol. The cells were centrifuged at 1000g for 5 min. The red blood cells were then lysed with 1× red blood cell (RBC) lysis buffer for 5 min at RT. The cells were centrifuged at 1000g for 5 min. The splenocytes were washed 3× with clean media.  $\sim$ 1.0  $\times$  10<sup>6</sup> cells were stained with anti-CD3-Pacific blue, anti-CD4-PE/ Cy7, anti-CD8a-FITC, anti-CD44-APC, and anti-CD62L-BV605 and analyzed by flow cytometry based on gating strategy in Figure S24.

Quantification of Lung Metastatic Nodules. Tumor-bearing mice were euthanized according to preferred institutional guidelines. Lungs were inflated with 10% India ink solution in Hanks' balanced salt solution (HBSS) through injection of 1 mL of solution using 25 G needle into trachea. After cutting away the connective tissue, the inflated lungs were transferred to a 50 mL conical tube containing 5 mL of Fekete's solution (35 mL of 95% EtOH, 15 mL of dH<sub>2</sub>O, 5 mL of formaldehyde, and 2.5 mL of glacial acetic acid) and incubated for 24 h at room temperature under a chemical fume hood. The lungs were removed, and the metastatic nodules were counted as white spots.

## ASSOCIATED CONTENT

## Supporting Information

The Supporting Information is available free of charge at https://pubs.acs.org/doi/10.1021/jacs.1c05090.

Experimental procedures, materials and methods, additional figures, and NMR spectra (PDF)

## AUTHOR INFORMATION

#### **Corresponding Authors**

Arezoo Shahrivarkevishahi – Department of Chemistry and Biochemistry, The University of Texas at Dallas, Richardson, Texas 75080, United States; Email: arezoo.shahrivar@gmail.com

Jeremiah J. Gassensmith — Department of Chemistry and Biochemistry and Department of Bioengineering, The University of Texas at Dallas, Richardson, Texas 75080, United States; orcid.org/0000-0001-6400-8106; Email: gassensmith@utdallas.edu

#### **Authors**

- Michael A. Luzuriaga Department of Chemistry and Biochemistry, The University of Texas at Dallas, Richardson, Texas 75080, United States; Present Address: Division of Infectious Diseases, Boston Children's Hospital, Division of Medical Sciences, Harvard Medical School, Boston, Massachusetts, U.S
- Fabian C. Herbert Department of Chemistry and Biochemistry, The University of Texas at Dallas, Richardson, Texas 75080, United States
- Alisia C. Tumac Department of Chemistry and Biochemistry, The University of Texas at Dallas, Richardson, Texas 75080, United States
- Olivia R. Brohlin Department of Chemistry and Biochemistry, The University of Texas at Dallas, Richardson, Texas 75080, United States; orcid.org/0000-0003-3226-6711
- **Yalini H. Wijesundara** Department of Chemistry and Biochemistry, The University of Texas at Dallas, Richardson, Texas 75080, United States
- Abhinay V. Adlooru Department of Chemistry and Biochemistry, The University of Texas at Dallas, Richardson, Texas 75080, United States
- Candace Benjamin Department of Chemistry and Biochemistry, The University of Texas at Dallas, Richardson, Texas 75080, United States
- Hamilton Lee Department of Chemistry and Biochemistry, The University of Texas at Dallas, Richardson, Texas 75080, United States; orcid.org/0000-0003-2176-925X
- Perouza Parsamian Department of Chemistry and Biochemistry, The University of Texas at Dallas, Richardson, Texas 75080, United States
- Jashkaran Gadhvi Department of Biological Sciences, The University of Texas at Dallas, Richardson, Texas 75080, United States
- Nicole J. De Nisco Department of Biological Sciences, The University of Texas at Dallas, Richardson, Texas 75080, United States; © orcid.org/0000-0002-7670-5301

Complete contact information is available at: https://pubs.acs.org/10.1021/jacs.1c05090

## **Author Contributions**

The manuscript was written by A.S and J.J.G. Synthesis, bioconjugation, PTPhage characterization, and *in vitro* studies were done by A.S. TEM image was done by O.R.B. Photothermal studies were performed by A.S, A.V.A., and A.C.T. Tumor implantation was done by A.S, M.A.L., and F.C.H. Histological analysis was done by A.S., F.C.H, A.V.A., J.G., and P.P. Flow Cytometry sample preparation was done by A.S, M.A.L, O.R.B, Y.H.W, A.V.A., and P.P.

## **Funding**

J.J.G. acknowledges National Science Foundation (Grants CAREER DMR-1654405 and DMR-2003534) and the Welch Foundation (Grant AT-1989-20190330). N.J.D. acknowledges the Welch Foundation (Grant AT-2030-20200401).

#### Notes

The authors declare no competing financial interest.

## ACKNOWLEDGMENTS

We thank Professor Paul Pantano and Dr. Ali Khademian for giving us the laser and all accoutrements. We thank Prof. Zhenpeng Qin and Yaning Liu for helpful discussions on photothermal conversion efficiency calculations. We thank Dr. Iman Yazdi for helpful discussions and review of our H&E stained pathology slides.

## ABBREVIATIONS

CCR2, CC chemokine receptor 2; CCL2, CC chemokine ligand 2; CCR5, CC chemokine receptor 5; TLC, thin layer chromatography

#### REFERENCES

- (1) Gao, D.; Guo, X.; Zhang, X.; Chen, S.; Wang, Y.; Chen, T.; Huang, G.; Gao, Y.; Tian, Z.; Yang, Z. Multifunctional phototheranostic nanomedicine for cancer imaging and treatment. *Materials Today Bio.* **2020**, *5*, 100035.
- (2) Chen, F.; Cai, W. Nanomedicine for targeted photothermal cancer therapy: where are we now? *Nanomedicine* **2015**, *10* (1), 1–3.
- (3) Pinto, A.; Pocard, M. Photodynamic therapy and photothermal therapy for the treatment of peritoneal metastasis: a systematic review. *Pleura Peritoneum* **2018**, 3 (4), 20180124–20180124.
- (4) Krysko, D. V.; Agostinis, P.; Krysko, O.; Garg, A. D.; Bachert, C.; Lambrecht, B. N.; Vandenabeele, P. Emerging role of damage-associated molecular patterns derived from mitochondria in inflammation. *Trends Immunol.* **2011**, 32 (4), 157–64.
- (5) Chen, G. Y.; Nunez, G. Sterile inflammation: sensing and reacting to damage. *Nat. Rev. Immunol.* **2010**, *10* (12), 826–37.
- (6) Hernandez, C.; Huebener, P.; Schwabe, R. F. Damage-associated molecular patterns in cancer: a double edged sword. *Oncogene* **2016**, 35 (46), 5931–5941.
- (7) West, C. L.; Doughty, A. C. V.; Liu, K.; Chen, W. R. Monitoring tissue temperature during photothermal therapy for cancer. *J. BioX Res.* **2019**, 2 (4), 159–168.
- (8) Li, L.; Yang, S.; Song, L.; Zeng, Y.; He, T.; Wang, N.; Yu, C.; Yin, T.; Liu, L.; Wei, X.; Wu, Q.; Wei, Y.; Yang, L.; Gong, C. An Endogenous Vaccine Based on Fluorophores and Multivalent Immunoadjuvants Regulates Tumor Micro-Environment for Synergistic Photothermal and Immunotherapy. *Theranostics* **2018**, *8* (3), 860–873.
- (9) Wang, C.; Xu, L.; Liang, C.; Xiang, J.; Peng, R.; Liu, Z. Immunological responses triggered by photothermal therapy with carbon nanotubes in combination with anti-CTLA-4 therapy to inhibit cancer metastasis. *Adv. Mater.* **2014**, *26* (48), 8154–62.
- (10) Sheng, W.; He, S.; Seare, W. J.; Almutairi, A. Review of the progress toward achieving heat confinement—the holy grail of photothermal therapy. *J. Biomed. Opt.* **2017**, 22 (8), 080901.
- (11) Yang, Z.; Sun, Z.; Ren, Y.; Chen, X.; Zhang, W.; Zhu, X.; Mao, Z.; Shen, J.; Nie, S. Advances in nanomaterials for use in photothermal and photodynamic therapeutics. *Mol. Med. Rep.* **2019**, 20 (1), 5–15.
- (12) Jaque, D.; Martinez Maestro, L.; del Rosal, B.; Haro-Gonzalez, P.; Benayas, A.; Plaza, J. L.; Martin Rodriguez, E.; Garcia Sole, J. Nanoparticles for photothermal therapies. *Nanoscale* **2014**, *6* (16), 9494–9530.
- (13) Lee, S.; George Thomas, R.; Ju Moon, M.; Ju Park, H.; Park, I.-K.; Lee, B. I.; Yeon Jeong, Y. Near-Infrared Heptamethine Cyanine Based Iron Oxide Nanoparticles for Tumor Targeted Multimodal Imaging and Photothermal Therapy. *Sci. Rep.* **2017**, *7* (1), 2108.
- (14) Wu, F.; Lu, Y.; Mu, X.; Chen, Z.; Liu, S.; Zhou, X.; Liu, S.; Li, Z. Intriguing H-Aggregates of Heptamethine Cyanine for Imaging-Guided Photothermal Cancer Therapy. ACS Appl. Mater. Interfaces 2020, 12 (29), 32388–32396.
- (15) Li, X.; Peng, X.-H.; Zheng, B.-D.; Tang, J.; Zhao, Y.; Zheng, B.-Y.; Ke, M.-R.; Huang, J.-D. New application of phthalocyanine molecules:

I

https://doi.org/10.1021/jacs.1c05090 J. Am. Chem. Soc. XXXX, XXX, XXX—XXX

- from photodynamic therapy to photothermal therapy by means of structural regulation rather than formation of aggregates. *Chem. Sci.* **2018**, *9* (8), 2098–2104.
- (16) Zheng, B.-D.; He, Q.-X.; Li, X.; Yoon, J.; Huang, J.-D. Phthalocyanines as contrast agents for photothermal therapy. *Coord. Chem. Rev.* **2021**, 426, 213548.
- (17) Cheung, C. C. L.; Ma, G.; Karatasos, K.; Seitsonen, J.; Ruokolainen, J.; Koffi, C.-R.; Hassan, H. A. F. M.; Al-Jamal, W. T. Liposome-Templated Indocyanine Green J- Aggregates for In Vivo Near-Infrared Imaging and Stable Photothermal Heating. *Nanotheranostics* **2020**, *4* (2), 91–106.
- (18) Holzer, W.; Mauerer, M.; Penzkofer, A.; Szeimies, R. M.; Abels, C.; Landthaler, M.; Baumler, W. Photostability and thermal stability of indocyanine green. *J. Photochem. Photobiol., B* **1998**, *47* (2), 155–164.
- (19) Vines, J. B.; Yoon, J.-H.; Ryu, N.-E.; Lim, D.-J.; Park, H. Gold Nanoparticles for Photothermal Cancer Therapy. *Front. Chem.* **2019**, *7*, 167–167.
- (20) Sobhani, Z.; Behnam, M. A.; Emami, F.; Dehghanian, A.; Jamhiri, I. Photothermal therapy of melanoma tumor using multiwalled carbon nanotubes. *Int. J. Nanomed.* **2017**, *12*, 4509–4517.
- (21) Estelrich, J.; Busquets, M. A. Iron Oxide Nanoparticles in Photothermal Therapy. *Molecules* **2018**, 23 (7), 1567.
- (22) Zhou, B.; Li, Y.; Niu, G.; Lan, M.; Jia, Q.; Liang, Q. Near-Infrared Organic Dye-Based Nanoagent for the Photothermal Therapy of Cancer. ACS Appl. Mater. Interfaces 2016, 8 (44), 29899–29905.
- (23) Avirah, R. R.; Jyothish, K.; Ramaiah, D. Infrared Absorbing Croconaine Dyes: Synthesis and Metal Ion Binding Properties. *J. Org. Chem.* **2008**, 73 (1), 274–279.
- (24) Lei, S.; Zhang, Y.; Blum, N. T.; Huang, P.; Lin, J. Recent Advances in Croconaine Dyes for Bioimaging and Theranostics. *Bioconjugate Chem.* **2020**, *31* (9), 2072–2084.
- (25) Tang, L.; Zhang, F.; Yu, F.; Sun, W.; Song, M.; Chen, X.; Zhang, X.; Sun, X. Croconaine nanoparticles with enhanced tumor accumulation for multimodality cancer theranostics. *Biomaterials* **2017**, *129*, 28–36.
- (26) Harmatys, K. M.; Battles, P. M.; Peck, E. M.; Spence, G. T.; Roland, F. M.; Smith, B. D. Selective photothermal inactivation of cells labeled with near-infrared croconaine dye. *Chem. Commun.* **2017**, 53 (71), 9906–9909.
- (27) Spence, G. T.; Hartland, G. V.; Smith, B. D. Activated photothermal heating using croconaine dyes. *Chem. Sci.* **2013**, *4* (11), 4240–4244.
- (28) Benjamin, C.; Brohlin, O.; Shahrivarkevishahi, A.; Gassensmith, J. J. Virus like particles: fundamental concepts, biological interactions, and clinical applications. In *Nanoparticles for Biomedical Applications*; Chung, E. J., Leon, L., Rinaldi, C., Eds.; Elsevier, 2020; Chapter 11, pp 153–174, DOI: 10.1016/B978-0-12-816662-8.00011-4.
- (29) Herbert, F. C.; Brohlin, O. R.; Galbraith, T.; Benjamin, C.; Reyes, C. A.; Luzuriaga, M. A.; Shahrivarkevishahi, A.; Gassensmith, J. J. Supramolecular Encapsulation of Small-Ultrared Fluorescent Proteins in Virus-Like Nanoparticles for Noninvasive In Vivo Imaging Agents. *Bioconjugate Chem.* **2020**, *31* (5), 1529–1536.
- (30) Wang, Q.; Lin, T.; Tang, L.; Johnson, J. E.; Finn, M. G. Icosahedral Virus Particles as Addressable Nanoscale Building Blocks. *Angew. Chem., Int. Ed.* **2002**, *41* (3), 459–462.
- (31) Chung, Y. H.; Cai, H.; Steinmetz, N. F. Viral nanoparticles for drug delivery, imaging, immunotherapy, and theranostic applications. *Adv. Drug Delivery Rev.* **2020**, *156*, 214–235.
- (32) Park, J.; Chariou, P. L.; Steinmetz, N. F. Site-Specific Antibody Conjugation Strategy to Functionalize Virus-Based Nanoparticles. *Bioconjugate Chem.* **2020**, *31* (5), 1408–1416.
- (33) Aanei, I. L.; Francis, M. B. Dual Surface Modification of Genome-Free MS2 Capsids for Delivery Applications. *Methods Mol. Biol.* **2018**, 1776, 629–642.
- (34) Purwar, M.; Pokorski, J. K.; Singh, P.; Bhattacharyya, S.; Arendt, H.; DeStefano, J.; La Branche, C. C.; Montefiori, D. C.; Finn, M. G.; Varadarajan, R. Design, display and immunogenicity of HIV1 gp120 fragment immunogens on virus-like particles. *Vaccine* **2018**, 36 (42), 6345–6353.

- (35) Benjamin, C. E.; Chen, Z.; Kang, P.; Wilson, B. A.; Li, N.; Nielsen, S. O.; Qin, Z.; Gassensmith, J. J. Site-Selective Nucleation and Size Control of Gold Nanoparticle Photothermal Antennae on the Pore Structures of a Virus. J. Am. Chem. Soc. 2018, 140 (49), 17226–17233.
- (36) Fiedler, J. D.; Fishman, M. R.; Brown, S. D.; Lau, J.; Finn, M. G. Multifunctional Enzyme Packaging and Catalysis in the Qβ Protein Nanoparticle. *Biomacromolecules* **2018**, 19 (10), 3945–3957.
- (37) Rampoldi, A.; Crooke, S. N.; Preininger, M. K.; Jha, R.; Maxwell, J.; Ding, L.; Spearman, P.; Finn, M. G.; Xu, C. Targeted Elimination of Tumorigenic Human Pluripotent Stem Cells Using Suicide-Inducing Virus-like Particles. *ACS Chem. Biol.* **2018**, *13* (8), 2329–2338.
- (38) Yin, Z.; Wu, X.; Kaczanowska, K.; Sungsuwan, S.; Comellas Aragones, M.; Pett, C.; Yu, J.; Baniel, C.; Westerlind, U.; Finn, M. G.; Huang, X. Antitumor Humoral and T Cell Responses by Mucin-1 Conjugates of Bacteriophage  $Q\beta$  in Wild-type Mice. ACS Chem. Biol. **2018**, *13* (6), 1668–1676.
- (39) Shoeb, E.; Hefferon, K. Future of cancer immunotherapy using plant virus-based nanoparticles. *Future Sci. OA* **2019**, *5* (7), FSO401–FSO401
- (40) Wang, C.; Fiering, S. N.; Steinmetz, N. F. Cowpea Mosaic Virus Promotes Anti-Tumor Activity and Immune Memory in a Mouse Ovarian Tumor Model. *Adv. Ther.* **2019**, 2 (5), 1900003.
- (41) Pitek, A. S.; Hu, H.; Shukla, S.; Steinmetz, N. F. Cancer Theranostic Applications of Albumin-Coated Tobacco Mosaic Virus Nanoparticles. *ACS Appl. Mater. Interfaces* **2018**, *10* (46), 39468–39477
- (42) Finbloom, J. A.; Han, K.; Aanei, I. L.; Hartman, E. C.; Finley, D. T.; Dedeo, M. T.; Fishman, M.; Downing, K. H.; Francis, M. B. Stable Disk Assemblies of a Tobacco Mosaic Virus Mutant as Nanoscale Scaffolds for Applications in Drug Delivery. *Bioconjugate Chem.* **2016**, 27 (10), 2480–2485.
- (43) Mohsen, M. O.; Speiser, D. E.; Knuth, A.; Bachmann, M. F. Virus-like particles for vaccination against cancer. *Wiley Interdiscip. Rev.: Nanomed. Nanobiotechnol.* **2020**, 12 (1), e1579.
- (44) Klimek, L.; Kundig, T.; Kramer, M. F.; Guethoff, S.; Jensen-Jarolim, E.; Schmidt-Weber, C. B.; Palomares, O.; Mohsen, M. O.; Jakob, T.; Bachmann, M. Virus-like particles (VLP) in prophylaxis and immunotherapy of allergic diseases. *Allergo J. Int.* **2018**, 27 (8), 245–255
- (45) Welch, R. P.; Lee, H.; Luzuriaga, M. A.; Brohlin, O. R.; Gassensmith, J. J. Protein-Polymer Delivery: Chemistry from the Cold Chain to the Clinic. *Bioconjugate Chem.* **2018**, *29* (9), 2867–2883.
- (46) Lee, H.; Shahrivarkevishahi, A.; Lumata, J. L.; Luzuriaga, M. A.; Hagge, L. M.; Benjamin, C. E.; Brohlin, O. R.; Parish, C. R.; Firouzi, H. R.; Nielsen, S. O.; Lumata, L. L.; Gassensmith, J. J. Supramolecular and biomacromolecular enhancement of metal-free magnetic resonance imaging contrast agents. *Chem. Sci.* **2020**, *11* (8), 2045–2050.
- (47) Dharmarwardana, M.; Martins, A. F.; Chen, Z.; Palacios, P. M.; Nowak, C. M.; Welch, R. P.; Li, S.; Luzuriaga, M. A.; Bleris, L.; Pierce, B. S.; Sherry, A. D.; Gassensmith, J. J. Nitroxyl Modified Tobacco Mosaic Virus as a Metal-Free High-Relaxivity MRI and EPR Active Superoxide Sensor. *Mol. Pharmaceutics* **2018**, *15* (8), 2973–2983.
- (48) Lin, S.; Liu, C.; Han, X.; Zhong, H.; Cheng, C. Viral Nanoparticle System: An Effective Platform for Photodynamic Therapy. *Int. J. Mol. Sci.* **2021**, 22 (4), 1728.
- (49) Rohovie, M. J.; Nagasawa, M.; Swartz, J. R. Virus-like particles: Next-generation nanoparticles for targeted therapeutic delivery. *Bioeng. Transl. Med.* **2017**, 2 (1), 43–57.
- (50) Chen, Z.; Boyd, S. D.; Calvo, J. S.; Murray, K. W.; Mejia, G. L.; Benjamin, C. E.; Welch, R. P.; Winkler, D. D.; Meloni, G.; D'Arcy, S.; Gassensmith, J. J. Fluorescent Functionalization across Quaternary Structure in a Virus-like Particle. *Bioconjugate Chem.* **2017**, 28 (9), 2277–2283.
- (51) Chen, Z.; Detvo, S. T.; Pham, E.; Gassensmith, J. J. Making Conjugation-induced Fluorescent PEGylated Virus-like Particles by Dibromomaleimide-disulfide Chemistry. *J. Visualized Exp.* **2018**, *135*, e57712.

- (52) Chen, Z.; Li, N.; Chen, L.; Lee, J.; Gassensmith, J. J. Dual Functionalized Bacteriophage  $Q\beta$  as a Photocaged Drug Carrier. *Small* **2016**, *12* (33), 4563–4571.
- (53) Chen, Z.; Li, N.; Li, S.; Dharmarwardana, M.; Schlimme, A.; Gassensmith, J. J. Viral chemistry: the chemical functionalization of viral architectures to create new technology. *Wiley Interdiscip. Rev.: Nanomed. Nanobiotechnol.* **2016**, 8 (4), 512–534.
- (54) Bear, A. S.; Kennedy, L. C.; Young, J. K.; Perna, S. K.; Mattos Almeida, J. P.; Lin, A. Y.; Eckels, P. C.; Drezek, R. A.; Foster, A. E. Elimination of metastatic melanoma using gold nanoshell-enabled photothermal therapy and adoptive T cell transfer. *PLoS One* **2013**, 8 (7), e69073.
- (55) Mohsen, M. O.; Gomes, A. C.; Vogel, M.; Bachmann, M. F. Interaction of Viral Capsid-Derived Virus-Like Particles (VLPs) with the Innate Immune System. *Vaccines* **2018**, *6* (3), 37.
- (56) Zepeda-Cervantes, J.; Ramirez-Jarquin, J. O.; Vaca, L. Interaction Between Virus-Like Particles (VLPs) and Pattern Recognition Receptors (PRRs) From Dendritic Cells (DCs): Toward Better Engineering of VLPs. Front. Immunol. 2020, 11, 1100.
- (57) Qian, C.; Liu, X.; Xu, Q.; Wang, Z.; Chen, J.; Li, T.; Zheng, Q.; Yu, H.; Gu, Y.; Li, S. Recent Progress on the Versatility of Virus-Like Particles. *Vaccines* **2020**, *8* (1), 139.
- (58) Song, X.; Foley, J. W. A new water-soluble near-infrared croconium dye. *Dyes Pigm.* **2008**, 78 (1), 60–64.
- (59) Liu, Y.; Ai, K.; Liu, J.; Deng, M.; He, Y.; Lu, L. Dopamine-Melanin Colloidal Nanospheres: An Efficient Near-Infrared Photo-thermal Therapeutic Agent for In Vivo Cancer Therapy. *Adv. Mater.* **2013**, 25 (9), 1353–1359.
- (60) Kang, P.; Chen, Z.; Nielsen, S. O.; Hoyt, K.; D'Arcy, S.; Gassensmith, J. J.; Qin, Z. Molecular Hyperthermia: Spatiotemporal Protein Unfolding and Inactivation by Nanosecond Plasmonic Heating. *Small* **2017**, *13* (36), 1700841.
- (61) Marabelle, A.; Andtbacka, R.; Harrington, K.; Melero, I.; Leidner, R.; de Baere, T.; Robert, C.; Ascierto, P. A.; Baurain, J. F.; Imperiale, M.; Rahimian, S.; Tersago, D.; Klumper, E.; Hendriks, M.; Kumar, R.; Stern, M.; Ohrling, K.; Massacesi, C.; Tchakov, I.; Tse, A.; Douillard, J. Y.; Tabernero, J.; Haanen, J.; Brody, J. Starting the fight in the tumor: expert recommendations for the development of human intratumoral immunotherapy (HIT-IT). *Ann. Oncol* **2018**, *29* (11), 2163–2174.
- (62) Steinman, R. M. Linking innate to adaptive immunity through dendritic cells. *Novartis Found. Symp.* **2006**, 279, 101–9 (discussion 109–13, 216–9).
- (63) Wculek, S. K.; Cueto, F. J.; Mujal, A. M.; Melero, I.; Krummel, M. F.; Sancho, D. Dendritic cells in cancer immunology and immunotherapy. *Nat. Rev. Immunol.* **2020**, *20* (1), 7–24.
- (64) Wang, J.; Chang, Y.; Luo, H.; Jiang, W.; Xu, L.; Chen, T.; Zhu, X. Designing immunogenic nanotherapeutics for photothermal-triggered immunotherapy involving reprogramming immunosuppression and activating systemic anti-tumor responses. *Biomaterials* **2020**, 255, 120153.
- (65) Guo, Y.; Ran, Y.; Wang, Z.; Cheng, J.; Cao, Y.; Yang, C.; Liu, F.; Ran, H. Magnetic-responsive and targeted cancer nanotheranostics by PA/MR bimodal imaging-guided photothermally triggered immunotherapy. *Biomaterials* **2019**, *219*, 119370.
- (66) Mellman, I.; Coukos, G.; Dranoff, G. Cancer immunotherapy comes of age. *Nature* **2011**, 480 (7378), 480–489.
- (67) Janeway, C. A., Jr.; Bottomly, K. Signals and signs for lymphocyte responses. *Cell* **1994**, *76* (2), 275–85.
- (68) Mohsen, M. O.; Gomes, A. C.; Vogel, M.; Bachmann, M. F. Interaction of Viral Capsid-Derived Virus-Like Particles (VLPs) with the Innate Immune System. *Vaccines* **2018**, *6* (3), 37.
- (69) Grgacic, E. V. L.; Anderson, D. A. Virus-like particles: passport to immune recognition. *Methods* **2006**, *40* (1), 60–65.
- (70) Kaczmarek, A.; Vandenabeele, P.; Krysko, D. V. Necroptosis: The Release of Damage-Associated Molecular Patterns and Its Physiological Relevance. *Immunity* **2013**, *38* (2), 209–223.
- (71) Xu, P.; Liang, F. Nanomaterial-Based Tumor Photothermal Immunotherapy. *Int. J. Nanomed.* **2020**, *15*, 9159–9180.

- (72) Cheng, H.-W.; Tsao, H.-Y.; Chiang, C.-S.; Chen, S.-Y. Advances in Magnetic Nanoparticle-Mediated Cancer Immune-Theranostics. *Adv. Healthcare Mater.* **2021**, *10* (1), 2001451.
- (73) O'Melia, M. J.; Rohner, N. A.; Manspeaker, M. P.; Francis, D. M.; Kissick, H. T.; Thomas, S. N. Quality of CD8+ T cell immunity evoked in lymph nodes is compartmentalized by route of antigen transport and functional in tumor context. *Sci. Adv.* **2020**, *6* (50), eabd7134.
- (74) Buchwald, Z. S.; Nasti, T. H.; Lee, J.; Eberhardt, C. S.; Wieland, A.; Im, S. J.; Lawson, D.; Curran, W.; Ahmed, R.; Khan, M. K. Tumordraining lymph node is important for a robust abscopal effect stimulated by radiotherapy. *JITC* **2020**, *8* (2), e000867.
- (75) Li, C.; Jiang, P.; Wei, S.; Xu, X.; Wang, J. Regulatory T cells in tumor microenvironment: new mechanisms, potential therapeutic strategies and future prospects. *Mol. Cancer* **2020**, *19* (1), 116.
- (76) Tormoen, G. W.; Crittenden, M. R.; Gough, M. J. Role of the immunosuppressive microenvironment in immunotherapy. *Adv. Radiat Oncol* **2018**, 3 (4), 520–526.
- (77) Lee, P. W.; Isarov, S. A.; Wallat, J. D.; Molugu, S. K.; Shukla, S.; Sun, J. E.; Zhang, J.; Zheng, Y.; Lucius Dougherty, M.; Konkolewicz, D.; Stewart, P. L.; Steinmetz, N. F.; Hore, M. J.; Pokorski, J. K. Polymer Structure and Conformation Alter the Antigenicity of Virus-like Particle-Polymer Conjugates. *J. Am. Chem. Soc.* **2017**, *139*, 3312–3315.